

Passive objects in confined active fluids: a localization transition

Ydan Ben Dor,¹ Yariv Kafri,¹ Mehran Kardar,² and Julien Tailleur³

¹*Department of Physics, Technion – Israel Institute of Technology, Haifa 32000, Israel*

²*Department of Physics, Massachusetts Institute of Technology, Cambridge, Massachusetts 02139, USA*

³*Université Paris Cité, Laboratoire Matière et Systèmes Complexes (MSC), UMR 7057 CNRS, F-75205 Paris, France*

We study how walls confining active fluids interact with asymmetric passive objects placed in their bulk. We show that the objects experience non-conservative long-ranged forces mediated by the active bath. To leading order, these forces can be computed using a generalized image theorem. The walls repel asymmetric objects, irrespective of their microscopic properties or their orientations. For circular cavities, we demonstrate how this may lead to the localization of asymmetric objects in the center of the cavity, something impossible for symmetric ones.

I. INTRODUCTION

Active matter describes systems comprising individual units that exert propelling forces on their environment [1–3]. Examples extend across scales, from molecular motors [4, 5] to animals [6, 7], including both biological [8, 9] and artificial systems [10, 11]. Active systems have attracted a lot of interest recently due to their rich collective behaviors [1, 12, 13] and to their non-trivial interactions with passive boundaries and objects [14–20]. Unlike in equilibrium settings, asymmetric objects generically induce long-ranged currents in active fluids which, in turn, mediate long-range interactions between inclusions [21, 22]. These currents have been shown to play an important role in the context of motility-induced phase separation [13] where random obstacles placed in the bulk of a system suppress phase separation in $d < 4$ dimensions [23]. Surprisingly, disordered obstacles localized on the boundaries also destroy phase separation in $d < 3$ dimensions [24], something impossible in equilibrium.

In this article, we study another surprising role of boundaries. In Figure 1, we show numerical simulations of an active fluid confined in a circular cavity in which a mobile asymmetric object has been inserted. Depending on the parameters, the object is either localized close to the cavity walls or in the middle of the cavity. As we show below, this is a direct consequence of the ratchet current induced by the object in the active bath and its interactions with the cavity walls. Note that, on general symmetry grounds, an isotropic object cannot be localized in a diffusive fluid. Indeed, the sole symmetry breaking field in the vicinity of an isotropic object is the gradient of the fluid density, $\nabla\rho$. The force \mathbf{F} exerted on the object thus satisfies $\mathbf{F} \propto \nabla\rho$. If the fluid is diffusive, it satisfies $\nabla^2\rho = 0$ in the steady state so that $\nabla \cdot \mathbf{F} = 0$ [25]. In analogy to Earnshaw’s theorem in electrostatics, this rules out the possibility of a stable equilibrium for the passive tracer. In contrast, an asymmetric polar object introduces a symmetry-breaking vector along which it generically generates a ratchet current [15–17, 21, 26]. This current is directly related to the non-vanishing mean force \mathbf{p} exerted by the object on the surrounding fluid [27]. Due to Newton’s third law, one thus generically expects a contribution to \mathbf{F} along

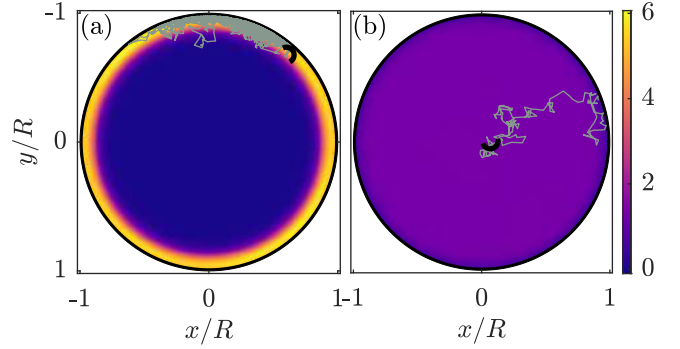


FIG. 1. Probability density of a semicircular mobile object surrounded by $N = 10^3$ non-interacting run-and-tumble particles confined to a circular cavity of unit diameter. Particle speed and tumbling rate are set to $v = 10^{-2}$ and $\alpha = 1$, respectively. The diameter of the semicircular object is equal to the particle persistence length $\ell_p = 10^{-2}$. The dynamics of the object is an overdamped Brownian motion at zero temperature with translational mobility set to unity and rotational mobility set to $\gamma = 10^2$ in (a) and $\gamma = 10^5$ in (b). The gray lines show typical trajectories of the object. The latter is displayed in black and enlarged by a factor of six. See Appendix A for numerical details.

– \mathbf{p} , which opens up the possibility of a localization transition. Figure 1 shows that this is indeed the case.

To uncover the mechanism behind this localization transition, we study the influence of boundaries on the coupling between asymmetric objects and active fluids. We start in Section II A by considering the case of an asymmetric polar object in the presence of a flat confining boundary. We show that the latter alters the far-field current and density modulation induced by the polar object, and that this effect can be rationalized using a generalized image theorem. As we show in Section II B, this leads to a repulsive force, which decays as a power-law, between the object and the wall. In Section III we then generalize our approach to the case of a polar object confined by a circular cavity. Finally, in Section IV, we consider a mobile object and show the existence of a localization transition. We note that our results could be tested experimentally by adapting a recent setup in which a *symmetric* object was immersed in a circular cav-

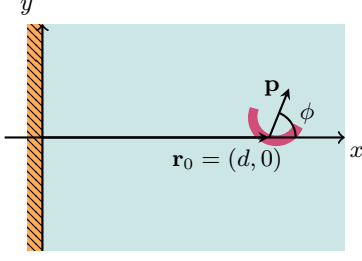


FIG. 2. An asymmetric passive object in an active fluid next to a flat wall at $x = 0$. The object is located at $\mathbf{r}_0 = (d, 0)$. Due to its asymmetric shape, it experiences a force $-\mathbf{p}$ from the active bath and thus exerts the opposite force \mathbf{p} on the active medium, whose orientation we denote by ϕ .

ity confining active colloids [20]. In this case, as expected on symmetry ground, no localization transition was observed and the interaction between the object and the wall is short ranged. We predict that employing a polar object should lead to rich physics. All derivations below are presented in two space dimensions but can easily be generalized to higher dimensions.

II. AN ASYMMETRIC OBJECT NEXT TO A FLAT WALL

We start by studying the influence of an infinite flat wall at $x = 0$ on an asymmetric object embedded inside the system in the neighborhood of $\mathbf{r}_0 = (d, 0)$ (see Fig. 2). We first determine in Sec. II A how the presence of the wall influences the ratchet current and the density modulation induced by the asymmetric object in the active bath. Then in Section II B, we show how the density modulation translates into a net nonconservative force exerted on the object. We characterize the force in the far field limit and show its magnitude to depend on the distance from the wall and on the orientation of the object.

In most of what follows, we focus on a dilute active bath. We thus solve for a single active particle that interacts with the obstacle and the boundaries. The average density for a bath comprising N active particles is then simply $\rho_N(\mathbf{r}) = N\rho(\mathbf{r})$ where $\rho(\mathbf{r})$ is the probability density of finding the active particle at position \mathbf{r} . For the flat-wall case discussed in this section, our results are generalized to particles interacting via pairwise forces in Appendix B.

To proceed, consider the master equation for the probability density $P_a(\mathbf{r}, \theta)$ to find an Active Brownian Particle (ABP) or a Run-and-Tumble particle (RTP) at $\mathbf{r} = (x, y)$ with orientation $\mathbf{u}(\theta) = (\cos \theta, \sin \theta)$:

$$\partial_t P_a(\mathbf{r}, \theta) = -\nabla \cdot [-\mu P_a \nabla U + v \mathbf{u} P_a - D_t \nabla P_a] + D_r \partial_\theta^2 P_a - \alpha P_a + \frac{\alpha}{2\pi} \int d\theta' P_a(\mathbf{r}, \theta'). \quad (1)$$

Here v is the self-propulsion speed of the active particle, μ its mobility, and D_t a translational diffusivity. The particle undergoes random reorientations with a (tumbling) rate α and rotational diffusion with an angular diffusivity D_r . The object is described by the external potential $U(\mathbf{r})$. In what follows we denote by $\tau = 1/(D_r + \alpha)$ and $\ell_p \equiv v\tau$ the particle's persistence time and length, respectively. The hard wall at $x = 0$ imposes a zero-flux condition:

$$-\mu P_a \partial_x U + v \cos \theta P_a - D_t \partial_x P_a = 0. \quad (2)$$

Integrating Eq. (1) over θ leads to a conservation equation for the density field $\rho(\mathbf{r}) = \int d\theta P_a(\mathbf{r}, \theta)$:

$$\partial_t \rho = -\nabla \cdot \mathbf{J}, \quad (3a)$$

$$\mathbf{J} = -\mu \rho \nabla U + v \mathbf{m} - D_t \nabla \rho, \quad (3b)$$

where $\mathbf{m} = \int d\theta \mathbf{u}(\theta) P_a(\mathbf{r}, \theta)$ is the polarization of the active particle and \mathbf{J} is the particle current in position space. The boundary condition (2) then translates into $J_x(x = 0, y) = 0$.

The dynamics of \mathbf{m} is then obtained by multiplying Eq. (1) by $\mathbf{u}(\theta)$ and integrating over θ , which gives:

$$\tau \partial_t \mathbf{m} = \frac{\mu}{v} \nabla \cdot \boldsymbol{\sigma}^a - \mathbf{m}, \quad (4)$$

where we have introduced the active stress tensor $\boldsymbol{\sigma}^a$ [18, 28–31]:

$$\sigma_{ij}^a = -\frac{v^2 \tau}{2\mu} \rho \delta_{ij} + \Sigma_{ij}, \quad (5a)$$

$$\Sigma_{ij} = -\frac{v\tau}{\mu} [v Q_{ij} - (\mu \partial_j U + D_t \partial_j) m_i]. \quad (5b)$$

Here $Q_{ij} = \int d\theta (u_i u_j - \delta_{ij}/2) P_a(\mathbf{r}, \theta)$ is the nematic tensor and we have singled out the contribution of the ideal gas pressure $v^2 \tau \rho / (2\mu)$ in the active stress tensor.

To determine the steady-state density profile, we first note that, on large length scales and long times, far from both the confining wall and the asymmetric object, the motion of the active particle is diffusive with a diffusion coefficient $D_{\text{eff}} = D_t + v^2 \tau / 2$. The corresponding probability current is then given by $\mathbf{J} \simeq -D_{\text{eff}} \nabla \rho$. As one moves closer to the object or the wall, this behavior is modified, which motivates us to define a residual field: the deviation \mathcal{J} from a diffusive current [24]

$$\mathcal{J} \equiv \mathbf{J} + D_{\text{eff}} \nabla \rho. \quad (6)$$

Using Eqs. (3)-(4) in the steady state where $\nabla \cdot \mathbf{J} = 0$, one finds that the density ρ satisfies

$$D_{\text{eff}} \nabla^2 \rho = \nabla \cdot \mathcal{J}, \quad (7a)$$

$$\mathcal{J}_i = -\mu \rho \partial_i U + \mu \partial_j \Sigma_{ij}. \quad (7b)$$

The zero-flux boundary condition on the current at $x = 0$ then reads

$$J_x(x = 0, y) = (\mathcal{J}_x - D_{\text{eff}} \partial_x \rho)|_{x=0} = 0. \quad (8)$$

A. Density profile and current

In the absence of the obstacle, the solution $\rho_{\text{FW}}(\mathbf{r})$ to Eq. (7) with the boundary condition (8) is a homogeneous bulk complemented by a finite-size boundary layer near the wall where active particles accumulate on a scale comparable to the persistence length ℓ_p [32]. In what follows, we denote by \mathcal{J}_{FW} the corresponding source term in Eq. (7b) and by Σ_{FW} the contribution (5b) to the active stress. By itself, determining ρ_{FW} is already a difficult problem, whose exact solution is not known [33–38]. To proceed, we thus work in the far field limit away from both the wall and the object, which is itself assumed to be far from the wall.

We first decompose the density field as $\rho(\mathbf{r}) = \rho_{\text{FW}}(\mathbf{r}) + \delta\rho(\mathbf{r})$ [39]. Thanks to the linearity of Poisson's equation (7), $\delta\rho$ satisfies

$$D_{\text{eff}} \nabla^2 \delta\rho = \nabla \cdot \delta\mathcal{J}, \quad (9a)$$

$$\delta\mathcal{J}_i = -\mu\rho\partial_i U + \partial_j \delta\Sigma_{ij}, \quad (9b)$$

where we have defined $\delta\mathcal{J} \equiv \mathcal{J} - \mathcal{J}_{\text{FW}}$, and $\delta\Sigma \equiv \Sigma - \Sigma_{\text{FW}}$. The corresponding boundary conditions read:

$$D_{\text{eff}} \partial_x \delta\rho|_{x=0} = \delta\mathcal{J}_x(0, y). \quad (10)$$

Equations (9)-(10) describe the density modulation created by the asymmetric object on the density profile induced by a flat wall. To solve for $\delta\rho(\mathbf{r})$, we introduce the Neumann-Green's function in the right half-plane:

$$G_N(\mathbf{r}; \mathbf{r}') = -\frac{1}{2\pi} \left[\ln \frac{|\mathbf{r} - \mathbf{r}'|}{\ell_p} + \ln \frac{|\mathbf{r}^\perp - \mathbf{r}'|}{\ell_p} \right]. \quad (11)$$

Here the term involving $\mathbf{r}^\perp = (-x, y)$ can be interpreted as a mirror image created on the other side of the wall. Note that the Neumann-Green's function (11) does not satisfy the boundary condition specified by Eq. (10), since its x -derivative vanishes on the boundary. Using Green's second identity [40, 41], this means that the solution $\delta\rho$ also includes a surface integral to enforce the

correct boundary condition. All in all, it reads

$$\begin{aligned} \delta\rho(x, y) &= -\frac{1}{D_{\text{eff}}} \int_0^\infty dx' \int_{-\infty}^\infty dy' G_N(x, y; x', y') \nabla' \cdot \delta\mathcal{J}' \\ &\quad - \int_{-\infty}^\infty dy' G_N(x, y; 0, y') \partial'_x \delta\rho' \Big|_{x'=0} \\ &= -\frac{\mu}{D_{\text{eff}}} \int_0^\infty dx' \int_{-\infty}^\infty dy' \rho' \nabla' U \cdot \nabla' G_N(x, y; x', y') \\ &\quad - \frac{\mu}{D_{\text{eff}}} \int_0^\infty dx' \int_{-\infty}^\infty dy' G_N(x, y; x', y') \partial'_i \partial'_j \delta\Sigma'_{ij} \end{aligned} \quad (12a)$$

$$- \frac{\mu}{D_{\text{eff}}} \int_0^\infty dx' \int_{-\infty}^\infty dy' G_N(x, y; x', y') \partial'_i \partial'_j \delta\Sigma'_{ij} \quad (12b)$$

$$- \frac{\mu}{D_{\text{eff}}} \int_{-\infty}^\infty dy' G_N(x, y; 0, y') \partial'_j \delta\Sigma'_{xj} \Big|_{x'=0}, \quad (12c)$$

where primed derivatives are taken with respect to x' and y' . To obtain Eq. (12) we use Eqs. (9) and (10) and an integration by parts. As we now show, the leading-order contribution to $\delta\rho$ in the far field is given by (12a). Noting that $\nabla' U$ is localized at $\mathbf{r}_0 = (d, 0)$, we approximate the Green's function as $\nabla' G_N(x, y; x', y') \simeq \nabla' G_N(x, y; x', y')|_{x'=d, y'=0}$ in the first integral. In the far field, where $|\mathbf{r} - \mathbf{r}_0|, d \gg a, \ell_p$ with a the size of the object, this leads to

$$\begin{aligned} \rho(\mathbf{r}) &\simeq \rho_b + \frac{\mu}{2\pi D_{\text{eff}}} \left[\frac{\mathbf{p} \cdot (\mathbf{r} - \mathbf{r}_0)}{|\mathbf{r} - \mathbf{r}_0|^2} + \frac{\mathbf{p}^\perp \cdot (\mathbf{r} - \mathbf{r}_0^\perp)}{|\mathbf{r} - \mathbf{r}_0^\perp|^2} \right] \\ &\quad + \mathcal{O}\left(|\mathbf{r} - \mathbf{r}_0|^{-2}, d^{-2}\right), \end{aligned} \quad (13)$$

where $\mathbf{p}^\perp = (-p_x, p_y)$ and we have used both that $\rho_{\text{FW}} \simeq \rho_b$ far from the wall and that $\mathbf{u} \cdot \mathbf{v} = \mathbf{u}^\perp \cdot \mathbf{v}^\perp$. In Eq. (13), \mathbf{p} is a force monopole defined by

$$\mathbf{p} = - \int d\mathbf{r} \rho \nabla U. \quad (14)$$

It measures the force exerted on the active fluid by the object in a system without a wall, whose exact value depends on microscopic details of U . Going back to Eq. (12), we show in appendix C that (12b) and (12c) are indeed negligible compared to (13). Intuitively, this relies both on the extra derivatives in Eq. (12b) and on the fact that we can use self-consistently the far-field approximation to $\delta\Sigma$ far away from the object.

The far-field currents can then be obtained from the above result. We first note that, outside the object, \mathcal{J} is negligible compared to the diffusive current $-D_{\text{eff}} \nabla \rho$

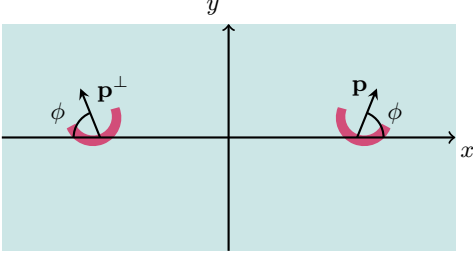


FIG. 3. The asymmetric object and the flat wall shown in Fig. 2 generate density modulations and currents in the active medium, far away from both the object and the wall, equivalent to those generated by two force monopoles \mathbf{p} and \mathbf{p}^\perp placed symmetrically with respect to the $x = 0$ plane.

(See Eq. (6)). One thus has that $\mathbf{J} = \mathcal{J} - D_{\text{eff}} \nabla \rho \simeq -D_{\text{eff}} \nabla \rho$ so that, to leading order:

$$\mathbf{J} \underset{|\mathbf{r}-\mathbf{r}_0|, d \gg a, \ell_p}{\simeq} \frac{\mu}{2\pi|\mathbf{r}-\mathbf{r}_0|^2} \left[\frac{2[(\mathbf{r}-\mathbf{r}_0) \cdot \mathbf{p}](\mathbf{r}-\mathbf{r}_0)}{|\mathbf{r}-\mathbf{r}_0|^2} - \mathbf{p} \right] + \frac{\mu}{2\pi|\mathbf{r}^\perp - \mathbf{r}_0|^2} \left[\frac{2[(\mathbf{r}-\mathbf{r}_0^\perp) \cdot \mathbf{p}^\perp](\mathbf{r}-\mathbf{r}_0^\perp)}{|\mathbf{r}-\mathbf{r}_0^\perp|^2} - \mathbf{p}^\perp \right]. \quad (15)$$

In summary, to this order of the multipole expansion, the problem of finding the steady-state density in the far field is reduced to a much simpler problem

$$D_{\text{eff}} \nabla^2 \rho = \mu \nabla \cdot [\mathbf{p} \delta(\mathbf{r} - \mathbf{r}_0)] , \quad (16a)$$

$$\partial_x \rho|_{x=0} = 0 , \quad (16b)$$

which amounts to Eqs. (9) and (10) with $\mathcal{J} \simeq \mu \mathbf{p} \delta(\mathbf{r} - \mathbf{r}_0)$. In the far field of both the object and the wall, the object thus appears as a force monopole \mathbf{p} at position \mathbf{r}_0 driving the fluid while the wall is equivalent to an image monopole \mathbf{p}^\perp at position \mathbf{r}_0^\perp , as can be read directly in Eq. (13) (see Fig. 3).

B. Nonconservative force induced on the object

According to Newton's third law, the object experiences a force $-\mathbf{p}$ from the active fluid. Equation (14) shows \mathbf{p} to depend on the local density of active particles $\rho(\mathbf{r})$, which in turn depends on the distance d from the wall through Eq. (13). It is thus convenient to decompose \mathbf{p} as:

$$\mathbf{p} \equiv \mathbf{p}_b - \mathbf{F} , \quad (17)$$

with \mathbf{p}_b defined as the value of \mathbf{p} when $d \rightarrow \infty$. Then \mathbf{F} measures the change in the force due to the presence of the wall. Namely, \mathbf{F} is the force induced on the object by the wall, which is mediated by the active bath.

Since the interaction with the wall is equivalent, to leading order, to the interaction with an image object, we can use the results of Refs. [21, 22] to derive \mathbf{F} . In

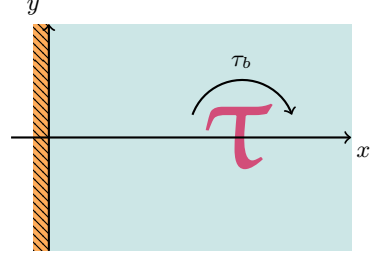


FIG. 4. A τ -shaped object generically experiences a non-zero self-torque τ_b .

the setting considered there, two objects, referred to as object 1 and object 2, are placed at positions \mathbf{r}_1 and \mathbf{r}_2 , with $\mathbf{r}_{12} \equiv \mathbf{r}_1 - \mathbf{r}_2$. When $|\mathbf{r}_{12}| \rightarrow \infty$ the objects experience forces $-\mathbf{p}_1$ and $-\mathbf{p}_2$ from the fluid, respectively. When $|\mathbf{r}_{12}|$ is finite the force experienced by object 1 is $-\mathbf{p}_1 + \mathbf{F}_{12}$, with \mathbf{F}_{12} the force exerted on object 1 due to the presence of object 2. In [21], it was shown that, to leading order in the far field, the interaction force arises due to a density modulation $\Delta\rho(\mathbf{r}_1)$ near object 1 due to object 2. This non-reciprocal interaction force takes the form:

$$\mathbf{F}_{12} = -\frac{\Delta\rho(\mathbf{r}_1)}{\rho_b} \mathbf{p}_1 , \quad (18)$$

with

$$\Delta\rho(\mathbf{r}_1) = \frac{\mu}{2\pi D_{\text{eff}}} \frac{\mathbf{r}_{12} \cdot \mathbf{p}_2}{|\mathbf{r}_{12}|^2} + \mathcal{O}(|\mathbf{r}_{12}|^{-2}) . \quad (19)$$

Here, $\mathbf{r}_{12} = (2d, 0)$ and $\mathbf{p}_2 = \mathbf{p}_b^\perp$ (see Fig. 3), leading to

$$\mathbf{F} = \frac{\mu}{2\pi D_{\text{eff}} \rho_b} \frac{p_{b,x}}{2d} \mathbf{p}_b + \mathcal{O}(d^{-2}) . \quad (20)$$

Denoting by ϕ the orientation of \mathbf{p}_b relative to the \mathbf{x} axis then leads to:

$$\mathbf{F} = \frac{\mu p_b^2}{8\pi D_{\text{eff}} \rho_b d} \begin{pmatrix} 1 + \cos(2\phi) \\ \sin(2\phi) \end{pmatrix} + \mathcal{O}(d^{-2}) , \quad (21)$$

with $p_b = |\mathbf{p}_b|$. Note that this result implies that the wall *always repels the object*, irrespective of its orientation ϕ . It is easy to check that $\partial_x F_y - \partial_y F_x \neq 0$, except when $\phi \in \{0, \pi\}$, so that the interaction force is not conservative [42].

Finally, an asymmetric object may also experience a torque from the surrounding active fluid [16, 17] (See Fig. 4). In two dimensions this torque is given by

$$\tau = \int_{\Omega} d\mathbf{r} \rho(\mathbf{r}) (\mathbf{r} - \mathbf{r}_{\text{CM}}) \times \nabla U , \quad (22)$$

where \mathbf{r}_{CM} is the object's center of mass. Denoting the magnitude of τ when $d \rightarrow \infty$ as τ_b and using the image

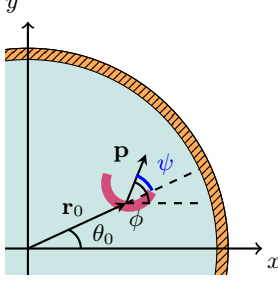


FIG. 5. An asymmetric passive object in an active fluid placed inside a circular cavity of radius R . The object is located at \mathbf{r}_0 at an angle θ_0 relative to the \hat{x} axis. The corresponding force monopole \mathbf{p} is directed along $\psi = \phi - \theta_0$ relative to \hat{r} .

object along with the results of Refs. [21, 22], we find that the interaction torque M due to the wall, defined through $\tau = \tau_b + M$, is given by

$$M = \frac{\mu p_b}{4\pi D_{\text{eff}} \rho_b} \frac{\cos(\phi)}{d} \tau_b + \mathcal{O}(d^{-2}). \quad (23)$$

Note that when the object is not chiral, τ_b vanishes and there is no torque to order $\mathcal{O}(d^{-1})$. Higher order contributions are, however, expected from symmetry considerations: the density modulation along \hat{x} due to the presence of the wall indeed breaks the chiral symmetry when \mathbf{p} is not along \hat{x} .

III. A OBJECT INSIDE A CIRCULAR CAVITY

In the previous section, we showed that, far from the object and away from a boundary layer created by a flat wall, the steady-state distribution and current of active particles are equivalent to those induced by two force monopoles placed symmetrically with respect to the plane of the wall. In turn, we showed that the object interacts with its mirror image, with an interaction force given by Eq. (20). We now consider a different setup of an asymmetric object placed in a circular cavity (See Fig. 5). We first determine in Section III A the long-ranged density modulation and current induced by object. Then, in Section III B, we compute the contribution of the force experienced by the object due to the circular confining boundary.

A. Density profile and current

Consider a passive asymmetric object placed inside an active fluid confined by a circular cavity of radius R . To make progress we assume that the far-field density modulation is given, to leading order, by the solution of Eq. (16) together with the Neumann boundary condition $\hat{r} \cdot \nabla \rho(\mathbf{r})|_{|\mathbf{r}|=R} = 0$. The Neumann-Green's function in

this geometry can be obtained in several ways, for example, by using conformal transformations or by using the polar symmetry of the domain. It is given by [40]

$$G_N^{\text{disk}}(\mathbf{r}; \mathbf{r}_0) = -\frac{1}{2\pi} [\ln(|\mathbf{r} - \mathbf{r}_0|/\ell_p) + \ln(|\mathbf{r} - \tilde{\mathbf{r}}_0|/\ell_p) + \ln(r_0/\ell_p)], \quad (24)$$

with $\tilde{\mathbf{r}}_0 \equiv (R/r_0)^2 \mathbf{r}_0$. Again, we write $\rho = \rho_b + \delta\rho$, with ρ_b the average density in the cavity. The leading order density modulation $\delta\rho(\mathbf{r})$ is then given in the far field by

$$\delta\rho \simeq -\frac{\mu}{2\pi D_{\text{eff}}} \left[\frac{(\mathbf{r} - \mathbf{r}_0) \cdot \mathbf{p}}{|\mathbf{r} - \mathbf{r}_0|^2} - \frac{(\mathbf{r} - \tilde{\mathbf{r}}_0) \cdot \tilde{\mathbf{p}}}{|\mathbf{r} - \tilde{\mathbf{r}}_0|^2} \right] + \frac{\mu \mathbf{r}_0 \cdot \mathbf{p}}{2\pi D_{\text{eff}} r_0^2}, \quad (25)$$

where $\tilde{\mathbf{p}} \equiv (R/r_0)^2 p \mathbf{u}(2\theta_0 - \phi)$. The diffusive current is then obtained using $\mathbf{J} \simeq -D_{\text{eff}} \nabla \rho$, leading to

$$\mathbf{J} \simeq \frac{\mu}{2\pi} \left[\frac{1}{|\mathbf{r} - \mathbf{r}_0|^2} \left(\frac{2[(\mathbf{r} - \mathbf{r}_0) \cdot \mathbf{p}](\mathbf{r} - \mathbf{r}_0)}{|\mathbf{r} - \mathbf{r}_0|^2} - \mathbf{p} \right) - \frac{1}{|\mathbf{r} - \tilde{\mathbf{r}}_0|^2} \left(\frac{2[(\mathbf{r} - \tilde{\mathbf{r}}_0) \cdot \tilde{\mathbf{p}}](\mathbf{r} - \tilde{\mathbf{r}}_0)}{|\mathbf{r} - \tilde{\mathbf{r}}_0|^2} - \tilde{\mathbf{p}} \right) \right]. \quad (26)$$

Again, the current in Eq. (26) is equivalent to that generated by the force monopole and an image monopole $\tilde{\mathbf{p}}$ placed at $\tilde{\mathbf{r}}_0$. The same applies to the density modulation, which also experiences an additional uniform contribution that enforces mass conservation.

We verified our predictions using numerical simulations of RTPs which are shown in Figure 6. Both density modulations and currents are well described by Eqs. (25) and (26).

B. Interaction force

Next we turn to derive the force induced on the object by the circular wall. To do this we first note that the presence of the wall leads to a density modulation

$$\Delta\rho(\mathbf{r}_0) \approx \frac{\mu}{2\pi D_{\text{eff}}} \left[\frac{\mathbf{r}_0}{r_0^2} \cdot \mathbf{p} + \frac{(\mathbf{r} - \tilde{\mathbf{r}}_0) \cdot \tilde{\mathbf{p}}}{|\mathbf{r} - \tilde{\mathbf{r}}_0|^2} \right] \Big|_{\mathbf{r}=\mathbf{r}_0}, \quad (27)$$

when compared to the situation in an infinite space. The force due to the presence of the wall is then given by Eq. (18), which leads to:

$$\mathbf{F} \approx -\frac{\mu p_b^2}{2\pi D_{\text{eff}} \rho_b} \frac{r_0 \cos(\phi - \theta_0)}{R^2 - r_0^2} \begin{pmatrix} \cos(\phi) \\ \sin(\phi) \end{pmatrix}, \quad (28)$$

with p_b the magnitude of the force monopole measured either in the center of the cavity or equivalently for $\tilde{r}_0 \rightarrow \infty$. As in the case of a flat wall, the force always repels the object away from the wall, as can be seen by setting $\theta_0 = 0$. Figure 7 shows a collapse of the force measured on the object for various orientations and distances from the wall, showing good agreement with the theory (28).

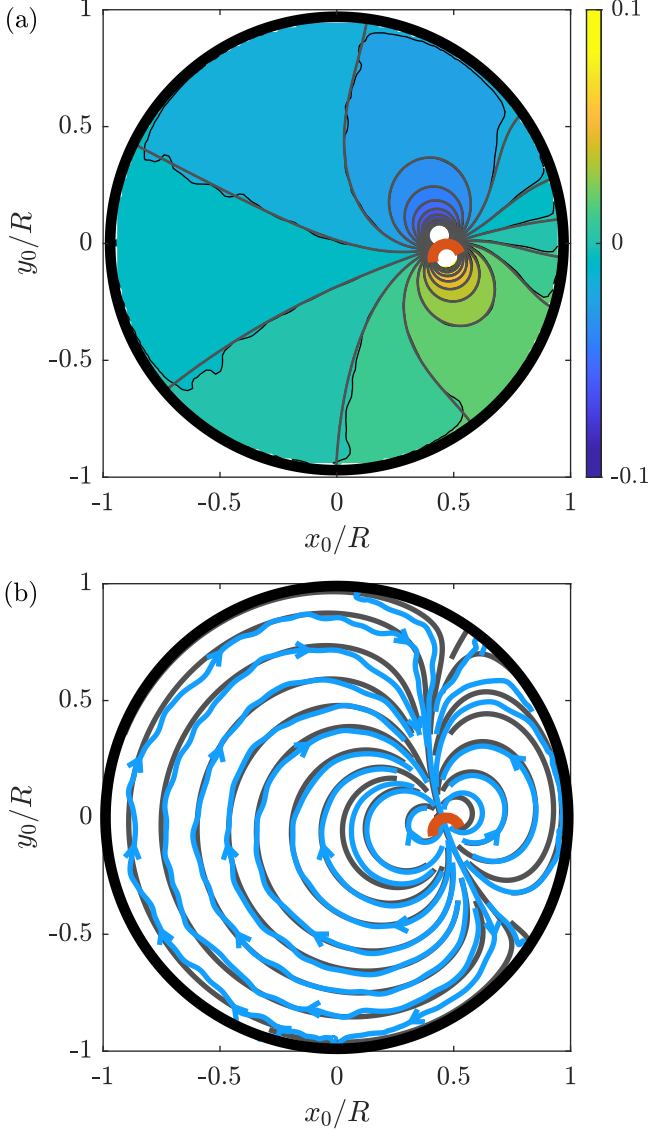


FIG. 6. Density and current profiles surrounding an asymmetric object inside a circular cavity. The object, shaped as a semicircular arc of diameter $d_{\text{arc}} = \ell_p$, is located at $\mathbf{r}_0 = (0.45R, 0)$ with an orientation making an angle $\phi = 0.6\pi$ with the \hat{x} axis. The object is displayed in orange and enlarged by a factor of six. (a) Steady-state density modulation relative to the bulk density, $\delta\rho/\rho_b$, compared with the analytical expression (25) in gray. (b) Streamlines of the steady-state current. The measurement (in light blue) is compared with the theory (in gray), for the same parameters as in (a). In both panels, the parameters were set as follows: $N = 10^5$ RTPs travel with speed $v = 10^{-4}$ and tumble at rate $\alpha = 10^{-2}$. See Appendix A for details.

Finally, as in the case of the flat wall, we can compute the interaction torque M acting on the object, which is given by

$$M \approx \frac{\mu p_b}{2\pi D_{\text{eff}} \rho_b} \frac{r_0 \cos(\phi - \theta_0)}{R^2 - r_0^2} \tau_b, \quad (29)$$

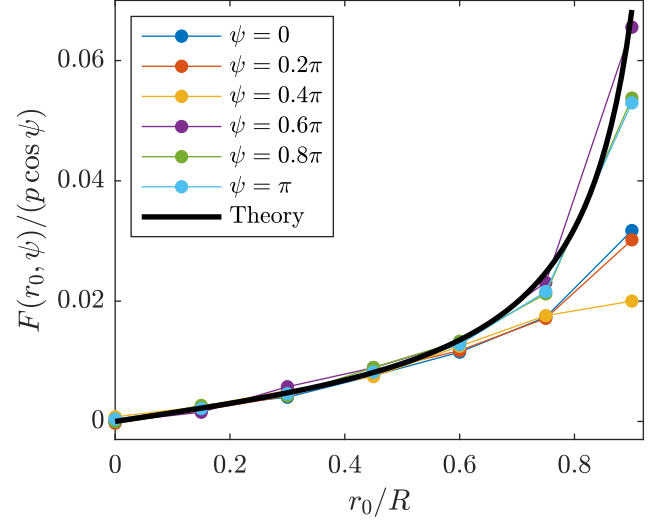


FIG. 7. Collapse of the interaction force exerted on the object. The data displayed here shows magnitude of the interaction force (28) divided by its angular dependence $\cos(\psi) = \cos(\phi - \theta_0)$ relative to the strength of the force monopole p . The solid black line shows the theoretical prediction with no parameter fitting. Note that the deviation from the theory near the walls is expected, due to higher-order interactions.

where τ_b is the object's self-torque measured at $r_0 = 0$.

IV. DYNAMICS OF AN ASYMMETRIC OBJECT INSIDE A CIRCULAR CAVITY

In the previous section, we computed the density modulation and current induced by a polar object held fixed in a circular cavity. The presence of confining walls leads to a renormalization of the force felt by the object which depends on its position and orientation. When the object is mobile, it is thus endowed with a non-uniform propulsion force. In this section we use a toy model to capture the corresponding dynamics and characterize its steady-state distribution. We find that the interaction with the wall leads to a transition between two distinct behaviors: the object is localized either in the center of the cavity or near the edges, as observed in Fig. 1.

To lighten the notations, we drop the subscript "0" when referring to the object so that its position reads $\mathbf{r} = r\mathbf{u}(\theta)$ and its orientation makes an angle ϕ with \hat{x} . We model the object's dynamics as an effective Langevin equation:

$$\dot{\mathbf{r}} = \mu_0 p \mathbf{u}(\phi) + \mu_0 \mathbf{F}(r, \theta, \phi) + \sqrt{2D_t^e} \boldsymbol{\eta}(t), \quad (30a)$$

$$\dot{\phi} = \sqrt{2D_r^e} \xi(t), \quad (30b)$$

where μ_0 is the mobility of the object, p is the magnitude of $-\mathbf{p}_b$, D_t^e and D_r^e are effective translational and rotational diffusivities, and $\eta_i(t)$ and $\xi(t)$ are Gaussian white noises of zero mean and unit variance. For simplicity, we consider a symmetric object whose self-torque is zero.

We now use the explicit expression of \mathbf{F} given in Eq. (28) and the angle $\psi = \phi - \theta$ between the object and $\hat{\mathbf{r}}$ (see Fig. 5) to rewrite Eq. (30) as a dynamics for r , θ and ψ . Since $r = \mathbf{r} \cdot \hat{\mathbf{r}}$, Itô calculus implies that $\dot{r} = \dot{\mathbf{r}} \cdot \hat{\mathbf{r}} + D_r^e/r$. Similar to the case of a particle in a harmonic well [43], the equations for r and ψ decouple from the dynamics of θ , and read:

$$\dot{r} = \mu_0 p \cos \psi \left[1 - \frac{qrR \cos(\psi)}{R^2 - r^2} \right] + \frac{D_r^e}{r} + \sqrt{2D_t^e} \eta_r(t), \quad (31a)$$

$$\dot{\psi} = -\frac{\mu_0 p \sin \psi}{r} \left[1 - \frac{qrR \cos(\psi)}{R^2 - r^2} \right] + \sqrt{2 \left(\frac{D_t^e}{r^2} + D_r^e \right)} \xi_\psi(t), \quad (31b)$$

where η_r and ξ_ψ are Gaussian white noises of zero mean and unit variance and $q = \mu p / (2\pi D_{\text{eff}} \rho_b R)$ is a dimensionless parameter.

Solving for the steady-state probability distribution $P(r, \psi)$ remains a hard task. Instead, we study the dynamics (31) in two limits: first when the object reorients so quickly that it is no longer persistent, $D_r^e \rightarrow \infty$, resulting in an effective equilibrium dynamics; and second, in the opposite limit, $D_r^e \rightarrow 0$, when the object is highly persistent. These two regimes lead to very different behaviors that explain the transition observed in Fig. 1.

Effective equilibrium limit. In the large D_r^e limit, the dynamics of ψ is dominated by the rotational diffusion, which leads to $P(r, \psi) \simeq P(r)/(2\pi)$. Taking the average of Eq. (31a) with respect to ψ then leads to:

$$\dot{r} = -\frac{\mu_0 p q r R}{2(R^2 - r^2)} + \frac{D_r^e}{r} + \sqrt{2D_t^e} \eta_r(t). \quad (32)$$

The steady-state distribution of r is then given by

$$P(r) \propto r \left(1 - \frac{r^2}{R^2} \right)^{\frac{\mu_0 p q R}{4D_t^e}}, \quad (33)$$

where $P(r)$ is normalized as $\int_0^R dr P(r) = 1$. Going back to the original \mathbf{r} variable, one thus gets

$$P(\mathbf{r}) \propto \left(1 - \frac{|\mathbf{r}|^2}{R^2} \right)^{\frac{\mu_0 p q R}{4D_t^e}}, \quad (34)$$

whose normalization in two dimensions reads $\int d\mathbf{r} P(\mathbf{r}) = 1$. Importantly, as can be seen in Fig. 8, the distribution is peaked around $\mathbf{r} = 0$ and perfectly matches microscopic simulations of Eq. (31). The result is reminiscent of the steady-state distribution of a run-and-tumble particle in a harmonic well in one space dimension [44, 45].

Finally, we note that this effective equilibrium regime allows for the localization of the object in the bulk of a non-equilibrium diffusive fluid. As mentioned in the introduction, this would be impossible in equilibrium due to Earnshaw's theorem. Here, when going from Eq. (31)

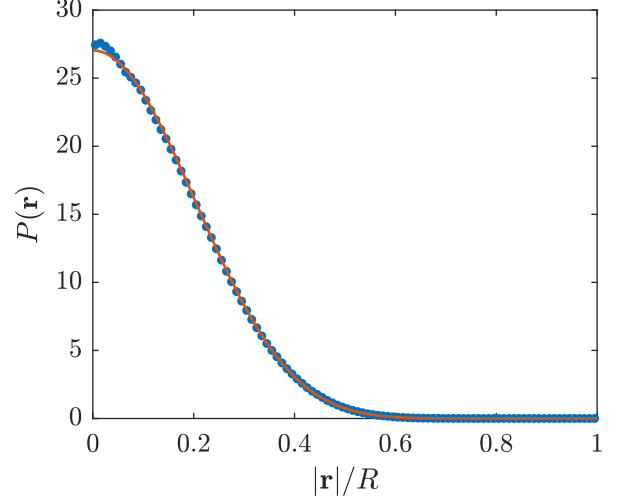


FIG. 8. Steady-state probability distribution $P(\mathbf{r})$ of the dynamics (31) in the large D_r^e limit. Direct simulations of the Langevin dynamics (31) (blue dots) agree perfectly with the analytic prediction of Eq. (34) (orange solid line).

to Eq. (32), the ‘bare’ self-propulsion force of the object has cancelled out and we are only left with the contribution from its image. The reason why the latter does not lead to a vanishing contribution is the strong anti-correlation between \mathbf{p} and its image.

Large-persistence regime. We now consider the opposite limit of a very small rotational diffusivity and set, for simplicity, $D_t^e = 0$. In this limit, the dynamics (31) reduce to:

$$\dot{r} = \mu_0 p \cos \psi \left[1 - \frac{qrR \cos(\psi)}{R^2 - r^2} \right], \quad (35a)$$

$$\dot{\psi} = -\frac{\mu_0 p \sin \psi}{r} \left[1 - \frac{qrR \cos(\psi)}{R^2 - r^2} \right]. \quad (35b)$$

Following [43], we expect that, in this noiseless limit, the object's position and orientation remain close to the stable fixed points of the dynamics (35), found by requiring $\partial_t r = \partial_t \psi = 0$. Direct inspection shows that all fixed points (r^*, ψ^*) satisfy

$$1 - \frac{qr^* R \cos(\psi^*)}{R^2 - (r^*)^2} = 0. \quad (36)$$

There is thus a continuous line of fixed points, which can be parameterized as $r^* = r^*(\psi^*)$:

$$r^*(\psi^*) = \frac{R}{2} \left(\sqrt{(q \cos \psi^*)^2 + 4} - q \cos \psi^* \right), \quad (37)$$

with $\psi^* \in [-\pi/2, \pi/2]$. The minimal value of $r^*(\psi^*)$ corresponds to $\psi^* = 0$ and $r^*(0) = \frac{R}{2}(\sqrt{q^2 + 4} - q) > 0$. This demonstrates that, in the steady state, the object is positioned at a finite distance from the origin, unlike in the effective equilibrium limit. By changing the rotational diffusion of the object, one can thus shift its most

probable localization from the center of the cavity to its periphery. Note that Eq. (35) relies on the far-field approximation, which is only valid far from the walls of confining boundaries. Ultimately, the only stable position of the object is at a distance close enough to the boundary that the modulation of the density of active particles is of order of ρ_b .

While the above discussion already proves the existence of the localization transition, we characterize, for completeness, the stability of the line of fixed points of the large persistence regime. As a first step, we linearize the dynamics (35) about $r^*(\psi^*)$. This yields a dynamical system that can be written as

$$\partial_t \begin{pmatrix} \delta r \\ \delta \psi \end{pmatrix} = M(\psi^*) \begin{pmatrix} \delta r \\ \delta \psi \end{pmatrix} + \mathcal{O}(\delta r^2, \delta \psi^2, \delta r \delta \psi), \quad (38)$$

for $\delta r \equiv r - r^*(\psi^*)$ and $\delta \psi \equiv \psi - \psi^*$, where

$$M_{11} = -\frac{\mu_0 p}{2qR} [4 + q \cos \psi^* \times \quad (39a)$$

$$\times \left(\sqrt{(q \cos \psi^*)^2 + 4} + q \cos \psi^* \right)],$$

$$M_{12} = \mu_0 p \sin \psi^*, \quad (39b)$$

$$M_{21} = \frac{\mu_0 p}{2qR^2} \left[2 \tan \psi^* \sqrt{(q \cos \psi^*)^2 + 4} + 4q \sin \psi^* \right. \\ \left. + \frac{q^2}{2} \sin(2\psi^*) \left(\sqrt{(q \cos \psi^*)^2 + 4} + q \cos \psi^* \right) \right] \quad (39c)$$

$$M_{22} = -\frac{2\mu_0 p}{R} \frac{\sin \psi^* \tan \psi^*}{\sqrt{(q \cos \psi^*)^2 + 4} - q \cos \psi^*}. \quad (39d)$$

Note that the matrix M depends on the value of ψ^* . For a given value of ψ^* , M can be diagonalized. Its eigenvectors point in two different directions: $\mathbf{v}_1(\psi^*)$ is tangent to the curve $r^*(\psi^*)$ and corresponds to a zero eigenvalue $\lambda_1 = 0$; $\mathbf{v}_2(\psi^*)$ points in a different direction and is associated to a negative eigenvalue λ_2 , given by

$$\lambda_2(\psi^*) = -\frac{\mu_0 p}{2qR} \left(4 + q^2 + q \frac{\sqrt{(q \cos \psi^*)^2 + 4}}{\cos \psi^*} \right). \quad (40)$$

The direction along the line of fixed point is thus, as expected, marginally stable, whereas the transverse direction is linearly stable. To find the most probable value of ψ^* and r^* , we thus need to go beyond the linear stability analysis and consider the non-linear dynamics of the perturbation along the line of fixed points.

To do so, we expand the evolution of $\delta \psi$, given by Eq. (35b), to second order in δr and $\delta \psi$. Imposing a perturbation tangent to the curve $r^*(\psi^*)$ then couples δr and $\delta \psi$. This leads to a closed dynamics for $\delta \psi$ given by

$$\partial_t \delta \psi = \Gamma(\psi^*) \delta \psi^2, \quad (41)$$

where $\Gamma(\psi^*)$ is given in Appendix A. Figure 9 shows that $\Gamma(\psi^*)$ and ψ^* have opposite signs so that $\psi^* = 0$ is the sole stable fixed point.

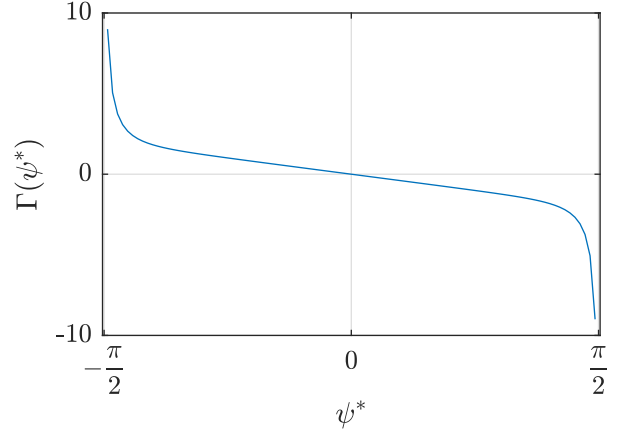


FIG. 9. $\Gamma(\psi^*)$ as a function of ψ^* , for $q = 0.5$. The exact expression is given in Appendix A. For $\psi^* > 0$, any perturbation $\delta \psi$ causes ψ^* to decrease. For $\psi^* < 0$, the opposite happens, leading to $\psi^* = 0$ as the sole stable fixed point.

In the steady state, we thus expect the object to point towards the wall, with $\psi = 0$, at a distance $r = \frac{R}{2}(\sqrt{q^2 + 4} - q)$ from the center of the cavity. Small deviations from this solution are expected mainly along the line of fixed points $r^*(\psi^*)$. This behavior is verified by a direct numerical simulation of Eq. (31) presented in Fig. 10.

All in all, the two limits of large and small rotational diffusivity show that there is a localization transition from a distribution where the object is localized close to the walls of the cavity to a distribution where the object is localized in its center. The latter occurs when the rotational diffusivity is large. Figure 11 shows the probability distributions of a polar object in a bath of active particles, measured numerically for the two regimes illustrated in Fig. 1, which indeed exhibits the corresponding transition.

V. CONCLUSION

In this manuscript we have considered the influence of boundaries on the motion of an asymmetric tracer in an active bath. Specifically, we have shown that the tracer experiences a non-conservative force mediated by the active medium, whose magnitude depends on the object's orientation. We then demonstrated how this force can be used to control the position of the object far in the bulk of the system.

To leading order, we have shown that the interaction with the walls can be accounted for using a generalized image theorem, which states that the passive object experiences long-range forces from its image. This holds despite the non-trivial boundary condition for the active fluid near the boundary. Using this result, we showed that, inside a circular cavity, two regimes can be observed depending on the parameters: either the object is con-

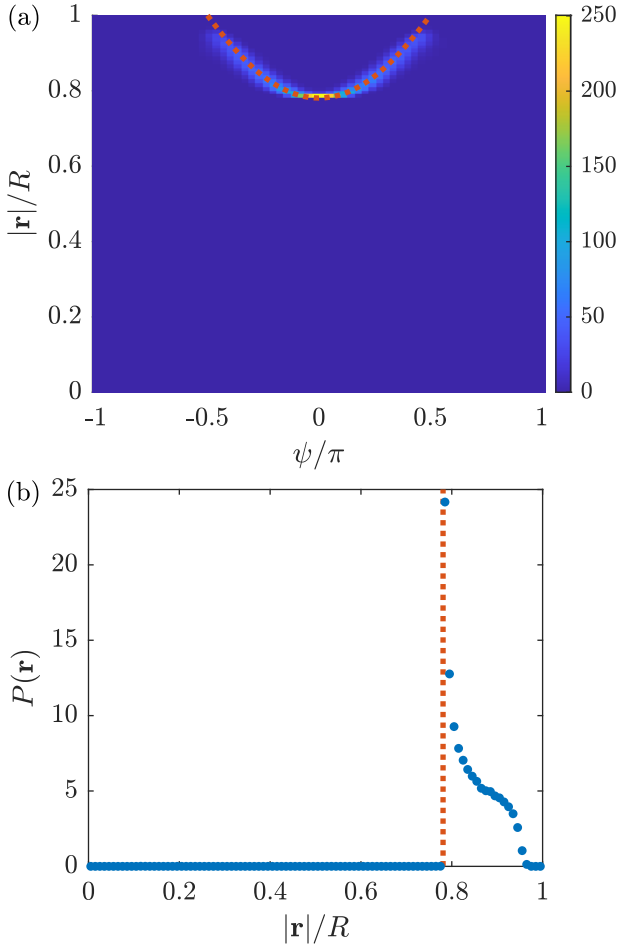


FIG. 10. Steady-state behavior of the object in the small D_r^e limit (with $D_t^e = 0$). (a) The probability distribution $P(\mathbf{r}, \psi)$ measured by direct simulations of the Langevin dynamics (31). The dotted orange line corresponds to the line of fixed points $r^*(\psi^*)$ given in Eq. (37). (b) The corresponding marginal probability density $P(\mathbf{r})$. The dotted orange line marks the expected position of the object when $D_r^e = 0$: $r = r^*(\psi = 0)$.

finned in the center of the cavity or it is localized close to its boundaries. All the results above are in sharp contrast to the case of a symmetric object where no stable minima can be found.

From a broader point of view, numerous mechanisms were suggested in the past to localize objects in the center of closed domains. This was studied extensively [46–49], in particular in the context of cell division [50, 51]. Our work offers a new, simple and generic mechanism to localize a passive object in the center of a circular region without requiring any exotic interactions. While simplistic in nature, this robust mechanism might play a role in such processes. It is tempting to search for additional applications of these forces, for instance to engineer passive objects that could be controlled by modifying the boundaries of the confining system. Finally, it would be

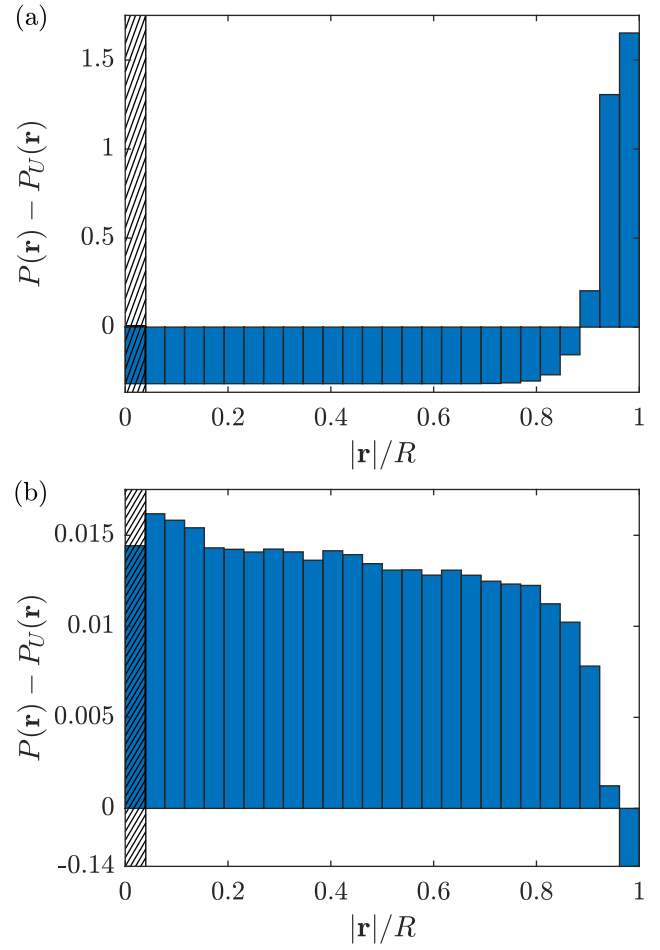


FIG. 11. Comparison between the probability density of the object's position $P(\mathbf{r})$ and a uniform distribution $P_U(\mathbf{r}) = 1/(\pi R^2)$ distribution. The two panels differ by the object's rotational mobility $\gamma = 10^2$ in (a) and $\gamma = 10^5$ in (b). The panels correspond to Figs. 1 (a) and (b), respectively. The shaded region indicates scales smaller than the object's diameter, where the sampling is expected to fail. See Appendix A for numerical details.

interesting to generalize our approach to domains of arbitrary shapes. The only non-trivial step seems to be the calculation of the Green's function, whose form can be derived using conformal mappings. This, however, is harder than it might seem since the Neumann boundary condition may introduce fictitious sources through the conformal mapping. A full generalization of our approach to general domains thus remains an open challenging problem.

ACKNOWLEDGMENTS

YBD and YK are supported by an Israel Science Foundation grant (2038/21). YBD, YK and MK are supported by an NSF5-BSF Grant No. DMR-170828008.

JT acknowledge the financial support of ANR grant THEMA.

Appendix A: Numerical methods

1. Numerical simulations of run-and-tumble dynamics with fixed obstacle

Since we consider non-interacting particles, their dynamics can be ran sequentially. Each particle propagates ballistically between the tumbles whose occurrence are drawn from an exponential distribution. The dynamics of the particle is time-stepped and we use $dt = 1$ and $v = 10^{-4}$. The collisions with walls and obstacles are then resolved exactly: when a particle displacement leads to a collision, the dynamics is integrated until the collision, and the particle then follows the boundary tangentially until the end of the time step or of the collision. Since we use (semi-)circular shapes for boundaries, this can be done analytically. Figure 12 illustrates the interactions of the particles with the object and the walls and shows typical trajectories obtained from the simulation. The force and the torque exerted by the particles on the object during their motion can also be derived analytically. For the force, the velocity component normal to the object is integrated over the duration of the particles' sliding motion.

2. Numerical simulations of run-and-tumble dynamics with moving object

The dynamics of the run-and-tumble particles are now computed in parallel. We also determine the torque exerted by the particles and set the object's axis of rotation to be at the midpoint between the two arc ends. In addition, the object now moves according to

$$\begin{aligned} \mathbf{r}(t + dt) &= \mathbf{r}(t) + \mu_0 \overline{\mathbf{f}} dt, \\ \phi(t + dt) &= \phi(t) + \gamma \overline{\tau} dt, \end{aligned} \quad (\text{A1})$$

where \mathbf{r} and ϕ are the positions and orientations of the object, and the integrated force and torques exerted by the particles during the time step dt are noted $\overline{\mathbf{f}} dt$ and $\overline{\tau} dt$, respectively.

3. Figures 1 & 11

To construct Fig. 1, the object's position was measured every 10^3 time-steps, binned in a $10^3 \times 10^3$ histogram, which was averaged over 500 realizations. The data were then smoothed using a Gaussian filter of width $\sigma_G = 1.5 \cdot 10^{-2} R$ with R the radius of the cavity. Typical trajectories of the objects (in black, enlarged by a factor of 6 for legibility) are displayed in gray. In Fig. 1(a),

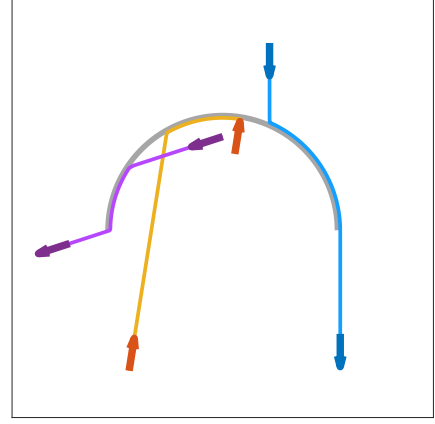


FIG. 12. Trajectories of a active particles modified by interactions, computed using the simulation. For clarity, the trajectories disregard tumble events, and so the particles are assumed to have constant velocities. A particle colliding with the outer, convex side of the semicircle (in blue) slides along the semicircle until it reaches its end. Afterwards, it continues with its original velocity. Particles colliding with the inner, concave side of the semicircle can have two different types of trajectories, depending on their orientation. One option (in purple) is that the particle slides along the inner side of the semicircle until it reaches its end. Then the particle continues its motion with its original velocity in the bulk of the cavity. Another option (in orange) is that the particle gets trapped inside the semicircle, stopping when its velocity is normal to semicircle. Trajectories similar to the latter occur also when the particle collides with the outer walls of the cavity.

the simulations ran for $t_f = 5 \cdot 10^7$. In Fig. 1(b), the simulations ran for $t_f = 2.2 \cdot 10^8$.

Figure 11 shows the radial probability distribution corresponding to the measurement shown in Fig. 1. The Cartesian two-dimensional distribution $P(x, y)$ was averaged over rings $r \leq \sqrt{x^2 + y^2} < (r + \Delta r)$ of constant thickness $\Delta r \approx 4 \cdot 10^{-2} R = 2\ell_p$. Below the scale set by the object size we encounter standard under-sampling problems due to the polar coordinates.

4. Figures 6 & 7

The data shown in the figures were averaged over 10 realizations, each running for a duration of $t_f = 5 \cdot 10^7$. All measurements were carried out after an initial transient of $t = 10^6$ time steps. Both figures were obtained using the same parameters.

To construct Fig. 6, the active particles' positions were stored and binned in a 400×400 histogram. In addition, their displacements during each time-step, divided by the time-step duration dt , were logged separately for the displacements along \hat{x} and \hat{y} on similar arrays. The data were then smoothed using a Gaussian filter of width $\sigma_G = 1.5 \cdot 10^{-2} R$ with R the radius of the cavity.

In Fig. 6(a), the density field was then fitted using Eq. (25) to extract the bulk density ρ_b , the position of the equivalent force monopole \mathbf{r}_0 and its value \mathbf{p} . The figure shows the measured density relative to the fitted bulk density ρ_b , in units of ρ_b . Gray and black solid lines show comparisons between predicted and measured iso-density lines. For clarity, the object is shown in orange, enlarged by a factor of 6.

Figure 6(b) shows streamlines of the measured current density in blue obtained using the Matlab tool streamslice. Using the measured strength and position of the force monopole we compare them with the predictions from Eq. (25) in gray.

In Fig. 7, to measure the force \mathbf{F} induced by the wall on the object, we first measured p_b by time-averaging the force exerted on an object placed at $\mathbf{r}_0 = 0$, where $\mathbf{F} = 0$, by symmetry.

We then measure the total force $-\mathbf{p}$ exerted on objects placed at various distances r from the center of the cavity, with different orientations ψ . We then added \mathbf{p}_b to this total force to extract the contribution \mathbf{F} from the wall, using Eq. (28).

Data measured for different values of ψ were collapsed by dividing \mathbf{F} by $\cos \psi$. Furthermore, the data are normalized by p_b . Our measurement of p_b agrees quantitatively with the fit done in Fig. 6. Finally, the solid black curve shows the dependence according to Eq. (28), obtained using the measurements of μp and ρ_b , measured in Fig. 6(a).

5. Figures 8 & 10

To produce the figures, the Langevin dynamics (31) were simulated using Euler time stepping with $dt = 10^{-1}$.

For Fig. 8, the steady-state distribution was obtained by binning r in 100 bins and dividing by the Jacobian r to get $P(\mathbf{r})$. The latter was then compared in the Figure with the prediction of Eq. (34). Parameters: $\mu_0 p = 10^{-4}$, $D_t^e = 10^{-6}$, $D_r^e = 10$, $q = 0.5$. Data were averaged over a total time of $t_f = 10^9$.

For Fig. 10, the steady-state distribution $P(\mathbf{r}, \psi)$ was done by binning the values of both r and ψ in a 100×64 array. P was again divided by the Jacobian r . Parameters: $\mu_0 p = 10^{-4}$, $D_r^e = 10^{-5}$, $q = 0.5$. The simulation was carried for a duration of $t_f = 10^8$.

6. Figure 9

The dynamics of $\delta\psi$ along the line of fixed points is given, to second order in $\delta\psi$ by:

$$\begin{aligned} \partial_t \delta\psi &\equiv \Gamma(\psi^*) \delta\psi^2 \\ &= \frac{\delta\psi^2}{4R} \tan \psi^* \left[2q(64 + 38q^2 + 5q^4) \right. \\ &\quad + q(256 + 112q^2 + 15q^4) \cos \psi^* \\ &\quad + 6q^3(6 + q^2) \cos(4\psi^*) + q^5 \cos(6\psi^*) \\ &\quad - 4\sqrt{(q \cos \psi^*)^2 + 4} \cos \psi^* \{ 32 + 3q^2(4 + q) \\ &\quad \left. + 4q^2(7 + q^2) \cos(2\psi^*) + q^4 \cos(4\psi^*) \} \right] \\ &\quad \times [(q \cos \psi^*)^2 + 4]^{-1} \\ &\quad \times \left[\sqrt{(q \cos \psi^*)^2 + 4} - q \cos \psi^* \right]^{-4}. \end{aligned} \quad (\text{A2})$$

Appendix B: Far-field density profile of pairwise-interacting active particles

In this Appendix, we generalize the proof of Section II to pairwise-interacting particles, showing they exhibit density and current profiles with the same functional form as non-interacting particles in the far field of both the object and the wall.

We start by considering the Langevin dynamics of the i^{th} active particle, located at \mathbf{r}_i with an orientation θ_i

$$\begin{aligned} \frac{d\mathbf{r}_i}{dt} &= v\mathbf{u}(\theta_i) - \mu\nabla \left[U(\mathbf{r}_i) + \sum_{j \neq i} u(|\mathbf{r}_i - \mathbf{r}_j|) \right] \\ &\quad + \sqrt{2D_t} \boldsymbol{\eta}_i(t), \end{aligned} \quad (\text{B1a})$$

$$\frac{d\theta_i}{dt} = \sqrt{2D_r} \xi_i(t). \quad (\text{B1b})$$

Here, on top of the dynamics in the dilute limit leading to Eq. (1), we add an isotropic inter-particle interaction potential $u(|\mathbf{r}_i - \mathbf{r}_j|)$. The particle's motion is subject to translational and rotational noises, $\xi_i(t)$ and $\boldsymbol{\eta}_i(t)$ respectively, which are assumed to be Gaussian, centered and of unit variances.

Using Itô calculus, one can derive the evolution equation of the empirical distribution $\Pi(\mathbf{r}, \theta, t) \equiv \sum_i \delta^{(2)}(\mathbf{r} - \mathbf{r}_i) \delta(\theta - \theta_i)$ of the active particles starting from dynamics (B1) [52]. Then, the evolution of the mean density $\rho(\mathbf{r}, t) \equiv \langle \hat{\rho}(\mathbf{r}, t) \rangle = \langle \sum_i \delta^{(2)}(\mathbf{r} - \mathbf{r}_i) \rangle$ can be derived, leading to a continuity equation in the steady state, similarly to Eqs. (3)-(5) in the dilute limit [22, 30, 53]:

$$\partial_t \rho = -\nabla \cdot \mathbf{J} = 0, \quad (\text{B2a})$$

$$\mathbf{J} = -\mu\rho\nabla U + \mu\nabla \cdot \boldsymbol{\sigma}, \quad (\text{B2b})$$

$$\sigma_{ij} = -\frac{D_{\text{eff}}}{\mu} \rho \delta_{ij} + \Sigma_{ij} + \sigma_{ij}^P + \sigma_{ij}^{\text{IK}}. \quad (\text{B2c})$$

Here Σ reads:

$$\Sigma_{ij} = -\frac{v\tau}{\mu} [vQ_{ij} - (\mu\partial_j U + D_t\partial_j) m_i], \quad (\text{B3})$$

where $m_k(\mathbf{r}, t) \equiv \langle \hat{m}_k(\mathbf{r}, t) \rangle = \langle \sum_i u_k(\theta) \delta^{(2)}(\mathbf{r} - \mathbf{r}_i) \rangle$ and $Q_{ij}(\mathbf{r}, t) \equiv \langle \sum_k [u_i(\theta) u_j(\theta) - \delta_{i,j}/2] \delta^{(2)}(\mathbf{r} - \mathbf{r}_k) \rangle$, $\boldsymbol{\sigma}^P$ is the tensor

$$\boldsymbol{\sigma}^P(\mathbf{r}) = \ell_p \int d^2 r' \nabla \mathbf{u}(|\mathbf{r} - \mathbf{r}'|) \langle \hat{\mathbf{m}}(\mathbf{r}) \hat{\rho}(\mathbf{r}') \rangle, \quad (\text{B4})$$

and $\boldsymbol{\sigma}^{\text{IK}}$ is the Irving-Kirkwood stress [54, 55]

$$\begin{aligned} \boldsymbol{\sigma}^{\text{IK}}(\mathbf{r}) = & \frac{1}{2} \int d^2 r' \frac{\mathbf{r}' \mathbf{r}'}{|\mathbf{r}'|} \mathbf{u}'(\mathbf{r}') \\ & \times \int_0^1 d\lambda \langle \hat{\rho}(\mathbf{r} + (1+\lambda)\mathbf{r}') \hat{\rho}(\mathbf{r} + (1-\lambda)\mathbf{r}') \rangle. \end{aligned} \quad (\text{B5})$$

As in the dilute limit derived in Section II, it is thus helpful to introduce a residual current

$$\mathcal{J}^\sigma \equiv \mathbf{J} - \mu \nabla \cdot \boldsymbol{\sigma}. \quad (\text{B6})$$

Using the steady-state equation $\nabla \cdot \mathbf{J} = 0$ then leads to

$$\mu \partial_i \partial_j \sigma_{ij} = -\partial_i \mathcal{J}_i^\sigma. \quad (\text{B7})$$

Furthermore, the no-flux boundary condition across the wall leads to:

$$J_x(0, y) = (\mu \partial_j \sigma_{xj} + \mathcal{J}_x^\sigma)|_{x=0} = 0. \quad (\text{B8})$$

Summation over repeated indices is implied henceforth. From there, we generalize for the stress tensor $\boldsymbol{\sigma}$ what we did for the density field in the main text.

We first employ a Helmholtz-Hodge decomposition for the stress-tensor's divergence

$$\nabla \cdot \boldsymbol{\sigma} \equiv -\nabla \Phi + \nabla \times \boldsymbol{\Psi}, \quad (\text{B9})$$

where $\boldsymbol{\Psi} \equiv \hat{\mathbf{z}} \Psi$ is a vector potential and Φ a scalar potential. With this, the tensor equation (B7) reduces to a Poisson equation, describing the scalar field Φ

$$\begin{aligned} \mu \nabla^2 \Phi &= \nabla \cdot \mathcal{J}^\sigma, \\ \mu \partial_x \Phi|_{x=0} &= (\mathcal{J}_x^\sigma + \mu \partial_y \Psi)|_{x=0}, \end{aligned} \quad (\text{B10})$$

similar to Eqs. (7)-(8) in the dilute limit.

In the absence of the object $U = 0$, the solution $\Phi_{\text{FW}}(\mathbf{r})$ to the boundary-value problem (B10) is uniform in the bulk of the system, with a finite-sized boundary layer close to the wall. We denote the quantities associated with this solution by Φ_{FW} , Ψ_{FW} , $\mathcal{J}_{\text{FW}}^\sigma$, and ρ_{FW} .

We now use the solution $\Phi_{\text{FW}}(\mathbf{r})$ to obtain the far-field behavior of the full solution $\Phi(\mathbf{r})$ in the presence of the object. To this end, we decompose Φ as $\Phi(\mathbf{r}) \equiv \Phi_{\text{FW}}(\mathbf{r}) + \delta\Phi(\mathbf{r})$ to find

$$\mu \nabla^2 \delta\Phi = \nabla \cdot \delta\mathcal{J}^\sigma, \quad (\text{B11a})$$

$$\delta\mathcal{J}_i^\sigma = -\mu \rho \partial_i U, \quad (\text{B11b})$$

$$\mu \partial_x \delta\Phi|_{x=0} = (\delta\mathcal{J}_x^\sigma + \mu \partial_y \delta\Psi)|_{x=0} = \mu \partial_y \delta\Psi|_{x=0}. \quad (\text{B11c})$$

Here $\delta\mathcal{J}^\sigma \equiv \mathcal{J}^\sigma - \mathcal{J}_{\text{FW}}^\sigma$ and $\delta\Psi \equiv \Psi - \Psi_{\text{FW}}$, thanks to the linearity of Poisson's equation. Equations (B11) describe the modulation $\delta\Phi$ created by an asymmetric object on top of the solution Φ_{FW} induced by the flat wall.

We can now readily use the Neumann-Green's function of the half-plane, given in Eq. (11), to solve the boundary value problem (B11). The solution reads

$$\begin{aligned} \mu \delta\Phi(\mathbf{r}) = & - \int_0^\infty dx' \int_{-\infty}^\infty dy' G_N(x, y; x', y') \nabla' \cdot \delta\mathcal{J}^{\sigma'} \\ & - \int_{-\infty}^\infty dy' G_N(x, y; 0, y') \mu \partial'_x \delta\Phi'|_{x'=0} \end{aligned} \quad (\text{B12})$$

Then, using Eq. (B11b) and performing an integration by parts, we get

$$\mu \delta\Phi(\mathbf{r}) = - \int_0^\infty dx' \int_{-\infty}^\infty dy' \mu \rho' \nabla' U \cdot \nabla' G_N(x, y; x', y') \quad (\text{B13a})$$

$$- \int_{-\infty}^\infty dy' G_N(x, y; 0, y') \mu \partial'_y \delta\Psi'|_{x'=0}. \quad (\text{B13b})$$

We now turn to evaluate this solution in the far field of both the object and the wall, where $(\mathbf{r} - \mathbf{r}_0), d \gg a, \ell_p$. As we show below, to leading order in the far field, $\delta\Phi$ is dominated by the integral (B13a) so that:

$$\begin{aligned} \delta\Phi(\mathbf{r})|_{|\mathbf{r}-\mathbf{r}_0|, d \gg a, \ell_p} \simeq & \frac{1}{2\pi} \cdot \left[\frac{\mathbf{p} \cdot (\mathbf{r} - \mathbf{r}_0)}{|\mathbf{r} - \mathbf{r}_0|^2} + \frac{\mathbf{p}^\perp \cdot (\mathbf{r} - \mathbf{r}_0^\perp)}{|\mathbf{r} - \mathbf{r}_0^\perp|^2} \right] \\ & + \mathcal{O}(|\mathbf{r} - \mathbf{r}_0|^{-2}, d^{-2}), \end{aligned} \quad (\text{B14})$$

where the force monopole \mathbf{p} has the same expression as in the dilute limit (14). As detailed in Ref. [22], it is possible to show that $\delta\Psi$ is of higher order compared to $\delta\Phi$. Namely, of order $\mathcal{O}(|\mathbf{r} - \mathbf{r}_0|^{-2}, d^{-2})$. Then, to leading order, $\sigma_{ij} \simeq \sigma_{\text{FW},ij} + \delta_{ij} \delta\Phi$. Furthermore, in the far field of the object, the stress tensor satisfies a local equation of state:

$$\boldsymbol{\sigma}(\mathbf{r}) = \boldsymbol{\sigma}(\rho(\mathbf{r})) + \mathcal{O}(\nabla \rho). \quad (\text{B15})$$

Denoting $\mathcal{P} = -\frac{1}{2} \text{Tr} \boldsymbol{\sigma}$ leads to $\mathcal{P}'(\rho_b) \delta\rho = \delta\Phi$, with $\mathcal{P}' = \partial\mathcal{P}/\partial\rho$ so that:

$$\begin{aligned} \delta\rho(\mathbf{r})|_{|\mathbf{r}-\mathbf{r}_0|, d \gg a, \ell_p} \simeq & \frac{\mathbf{p}}{2\pi \mathcal{P}'(\rho_b)} \cdot \left[\frac{\mathbf{r} - \mathbf{r}_0}{|\mathbf{r} - \mathbf{r}_0|^2} + \frac{\mathbf{r}^\perp - \mathbf{r}_0^\perp}{|\mathbf{r}^\perp - \mathbf{r}_0^\perp|^2} \right] \\ & + \mathcal{O}(|\mathbf{r} - \mathbf{r}_0|^{-2}, d^{-2}). \end{aligned} \quad (\text{B16})$$

Appendix C: Validity of the multipole expansion

Here we show that Eqs. (12b)-(12c) are indeed negligible compared to (12a) in the far field of both the object

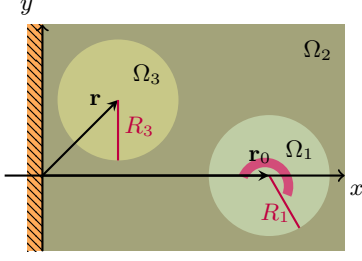


FIG. 13. Regions Ω_o , enclosing the object, and Ω_o^c .

and the wall. For legibility, we remind here the full expression of the integral:

$$\delta\rho(x, y) = -\frac{\mu}{D_{\text{eff}}} \int_0^\infty dx' \int_{-\infty}^\infty dy' \rho' \nabla' U \cdot \nabla' G_N(x, y; x', y') \quad (\text{C1a})$$

$$-\frac{\mu}{D_{\text{eff}}} \int_0^\infty dx' \int_{-\infty}^\infty dy' G_N(x, y; x', y') \partial'_i \partial'_j \delta\Sigma'_{ij} \quad (\text{C1b})$$

$$-\frac{\mu}{D_{\text{eff}}} \int_{-\infty}^\infty dy' G_N(x, y; 0, y') \partial'_j \delta\Sigma'_{xj} \Big|_{x'=0}. \quad (\text{C1c})$$

The main difficulty of the argument stems from the non-local structure of $\delta\Sigma$ which is non-vanishing across the entire space accessible to the active fluid. To proceed, we divide the half-plane in three regions: Ω_1 is a disk of radius R_1 centered on the object, Ω_3 is a disk of radius R_3 centered on the position \mathbf{r} where the density field is evaluated, and Ω_2 is the complement to $\Omega_1 \cup \Omega_3$ (see Fig. 13). For reasons that will become clear later on, we set $R_3 = \varepsilon|\mathbf{r} - \mathbf{r}_0|$, with ε a constant less than 1/2. We also set R_1 to be large enough that all fields outside Ω_1 can be evaluated using their far-field multipolar expressions.

Integrating by parts Eq. (C1b) first cancels the contribution of Eq. (C1c). A second integration by parts leads to

$$-\frac{\mu}{D_{\text{eff}}} \int_0^\infty dx' \int_{-\infty}^\infty dy' \partial'_i \partial'_j G_N(x, y; x', y') \delta\Sigma'_{ij}. \quad (\text{C2})$$

The lack of any other boundary term is due to the boundary conditions on the Green's function and on $\delta\Sigma$.

We start by discussing the region Ω_1 enclosing the object and its contribution to Eq. (C2). As Ω_1 is closed and finite, one can treat $\delta\Sigma$ in this region as a localized source density. It is thus possible to perform a multipole expansion to compute its contribution to the density modulation and current at a position \mathbf{r} in the far field. The

integral over Ω_1 has one more derivative—and is hence of a higher order—than the contribution of Eq. (C1a).

Before we turn to the regions Ω_2 and Ω_3 , we note that Eq. (5b) implies that $\delta\Sigma$ is given by

$$\delta\Sigma_{ij} \Big|_{\mathbf{r} \in \Omega_1^c} = -\frac{v\tau}{\mu} [v\delta Q_{ij} - D_i \partial_j \delta m_i] \quad (\text{C3})$$

in the region $\Omega_1^c = \Omega_2 \cup \Omega_3$. By construction, in this region, $\delta\mathbf{m}$ and $\delta\mathbf{Q}$ take their far-field forms. Then, Eqs. (1) and (4) show that $\delta\mathbf{m} \sim \nabla\rho$ and $\delta\mathbf{Q} \sim \nabla\nabla\rho$. Using the density profile (13) self-consistently, we thus find

$$\delta\Sigma \Big|_{\mathbf{r} \in \Omega_1^c} \sim \frac{1}{|\mathbf{r} - \mathbf{r}_0|^3}, \quad (\text{C4})$$

to leading order in the far field. Note that the contributions for the image object follow the same scaling.

Let us now turn to the region Ω_3 . There, an apparent singularity at $\mathbf{r} = \mathbf{r}'$ requires some care. We thus integrate by parts Eq. (C2) to get:

$$-\frac{\mu}{D_{\text{eff}}} \int_{\partial\Omega_3} d^2\mathbf{r}' \partial'_j G_N(x, y; x', y') \delta\Sigma'_{ij} \quad (\text{C5})$$

$$+\frac{\mu}{D_{\text{eff}}} \int_{\Omega_3} d^2\mathbf{r}' \partial'_j G_N(x, y; x', y') \partial'_i \delta\Sigma'_{ij}. \quad (\text{C6})$$

Let us first look at the boundary term. On $\partial\Omega_3$, $|\mathbf{r}' - \mathbf{r}_0| > |\mathbf{r} - \mathbf{r}_0|/2$ so that $|\delta\Sigma'_{ij}|$ decays asymptotically as $\mathcal{O}(|\mathbf{r} - \mathbf{r}_0|^{-3})$. Furthermore, the gradient of the Green's function scales as $|\partial'_i G_N| \sim R_3^{-1}$. Overall, the boundary integral can thus be controlled as:

$$\int_{\partial\Omega_3} d^2\mathbf{r}' \partial'_j G_N(x, y; x', y') \delta\Sigma'_{ij} = \mathcal{O}\left(\frac{P(\Omega_3)}{R_3} \frac{1}{|\mathbf{r} - \mathbf{r}_0|^3}\right),$$

where $P(\Omega_3) = 2\pi R_3$ is the length of $\partial\Omega_3$. This integral is thus negligible compared to the contribution of Eq. (C1a).

To estimate Eq. (C6), we note that it can be estimated as

$$\int_{\Omega_3} d^2\mathbf{r}' [\partial'_j G_N(\mathbf{r}; \mathbf{r}')] [\partial'_i \delta\Sigma'_{ij}] \sim \int_{\Omega_3} \frac{d^2\mathbf{r}'}{|\mathbf{r} - \mathbf{r}'|^4} \frac{1}{|\mathbf{r}' - \mathbf{r}_0|^4}. \quad (\text{C7})$$

To show that there is no divergence at $\mathbf{r} = \mathbf{r}'$ we change variable to $\mathbf{u} \equiv \mathbf{r} - \mathbf{r}'$. With this, Eq. (C7) becomes

$$\int_{\Omega_3} \frac{u du d\gamma}{u} \frac{1}{|\mathbf{r} - \mathbf{r}_0 - \mathbf{u}|^4}, \quad (\text{C8})$$

with $u = |\mathbf{u}|$ and $\tan \gamma = u_y/u_x$, showing that the $u \rightarrow 0$ limit is regular. The $|\mathbf{r} - \mathbf{r}_0|^4$ scaling then shows the contribution of Eq. (C7) to be negligible compared to Eq. (C1a).

We are finally left with the integral over region Ω_2 , which scales as

$$\int_{\Omega_2} d^2\mathbf{r}' [\partial'_i \partial'_j G_N(\mathbf{r}; \mathbf{r}')] \delta\Sigma_{ij} \sim \int_{\Omega_2} \frac{d^2\mathbf{r}'}{|\mathbf{r} - \mathbf{r}'|^2} \frac{1}{|\mathbf{r}' - \mathbf{r}_0|^3}. \quad (\text{C9})$$

Since, in this region, $|\mathbf{r} - \mathbf{r}'| > R_3$, this integral is smaller than:

$$\frac{1}{R_3^2} \int_{\Omega_2} \frac{d^2 \mathbf{r}'}{|\mathbf{r}' - \mathbf{r}_0|^3}. \quad (\text{C10})$$

The last integral can then be extended over the complementary to Ω_1 in \mathbb{R}^2 , leading to a contribution smaller than

$$\left| \int_{\Omega_2} d^2 \mathbf{r}' [\partial_i \partial_j G_N(\mathbf{r}; \mathbf{r}')] \delta \Sigma_{ij} \right| \lesssim \frac{1}{R_1 R_3^2}. \quad (\text{C11})$$

Since $R_3 = \varepsilon |\mathbf{r} - \mathbf{r}_0|$, this final contribution is also negligible compared to Eq. (C1a). This concludes our demonstration that Eq. (C1a) is, self-consistently, the dominating contribution to the density modulation.

-
- [1] M. Marchetti, J. Joanny, S. Ramaswamy, T. Liverpool, J. Prost, M. Rao, and T. Aditi Simha, Hydrodynamics of soft active matter, *Reviews of Modern Physics* **85**, 1143 (2013).
 - [2] C. Bechinger, R. Di Leonardo, H. Löwen, C. Reichhardt, G. Volpe, and G. Volpe, Active particles in complex and crowded environments, *Reviews of Modern Physics* **88**, 045006 (2016).
 - [3] J. O'Byrne, Y. Kafri, J. Tailleur, and F. van Wijland, Time irreversibility in active matter, from micro to macro, *Nature Reviews Physics*, 1 (2022).
 - [4] V. Schaller, C. Weber, C. Semmrich, E. Frey, and A. R. Bausch, Polar patterns of driven filaments, *Nature* **467**, 73 (2010).
 - [5] T. Sanchez, D. T. Chen, S. J. DeCamp, M. Heymann, and Z. Dogic, Spontaneous motion in hierarchically assembled active matter, *Nature* **491**, 431 (2012).
 - [6] M. Ballerini, N. Cabibbo, R. Candelier, A. Cavagna, E. Cisbani, I. Giardina, V. Lecomte, A. Orlandi, G. Parisi, A. Procaccini, *et al.*, Interaction ruling animal collective behavior depends on topological rather than metric distance: Evidence from a field study, *Proceedings of the national academy of sciences* **105**, 1232 (2008).
 - [7] D. S. Calovi, U. Lopez, S. Ngo, C. Sire, H. Chaté, and G. Theraulaz, Swarming, schooling, milling: phase diagram of a data-driven fish school model, *New journal of Physics* **16**, 015026 (2014).
 - [8] D. Bi, X. Yang, M. C. Marchetti, and M. L. Manning, Motility-driven glass and jamming transitions in biological tissues, *Physical Review X* **6**, 021011 (2016).
 - [9] D. Matoz-Fernandez, E. Agoritsas, J.-L. Barrat, E. Bertin, and K. Martens, Nonlinear rheology in a model biological tissue, *Physical review letters* **118**, 158105 (2017).
 - [10] D. Geyer, D. Martin, J. Tailleur, and D. Bartolo, Freezing a flock: Motility-induced phase separation in polar active liquids, *Physical Review X* **9**, 031043 (2019).
 - [11] M. N. Van Der Linden, L. C. Alexander, D. G. Aarts, and O. Dauchot, Interrupted motility induced phase separation in aligning active colloids, *Physical review letters* **123**, 098001 (2019).
 - [12] T. Vicsek, A. Czirók, E. Ben-Jacob, I. Cohen, and O. Shochet, Novel Type of Phase Transition in a System of Self-Driven Particles, *Physical Review Letters* **75**, 1226 (1995).
 - [13] M. E. Cates and J. Tailleur, Motility-Induced Phase Separation, *Annual Review of Condensed Matter Physics* **6**, 219 (2015).
 - [14] P. Galajda, J. Keymer, P. Chaikin, and R. Austin, A wall of funnels concentrates swimming bacteria, *Journal of bacteriology* **189**, 8704 (2007).
 - [15] J. Tailleur and M. Cates, Sedimentation, trapping, and rectification of dilute bacteria, *EPL* **86**, 600002 (2009).
 - [16] A. Sokolov, M. Apodaca, B. Grzybowski, and I. Aranson, Swimming bacteria power microscopic gears, *Proceedings of the National Academy of Sciences* **107**, 969 (2010).
 - [17] R. Di Leonardo, L. Angelani, D. Dell Arciprete, G. Ruocco, V. Iebba, S. Schippa, M. P. Conte, F. Mecarini, F. De Angelis, and E. Di Fabrizio, Bacterial ratchet motors, *Proceedings of the National Academy of Sciences* **107**, 9541 (2010).
 - [18] A. Solon, Y. Fily, A. Baskaran, M. Cates, Y. Kafri, M. Kardar, and J. Tailleur, Pressure is not a state function for generic active fluids, *Nature Physics* **11**, 673 (2015).
 - [19] O. Granek, Y. Kafri, and J. Tailleur, The anomalous transport of tracers in active baths, *arXiv preprint arXiv:2108.11970* (2021).
 - [20] S. Paul, A. Jayaram, N. Narinder, T. Speck, and C. Bechinger, Force generation in confined active fluids: The role of microstructure, *arXiv preprint arXiv:2205.05619* (2022).
 - [21] Y. Baek, A. Solon, X. Xu, N. Nikola, and Y. Kafri, Generic long-range interactions between passive bodies in an active fluid, *Physical review letters* **120**, 058002 (2018).
 - [22] O. Granek, Y. Baek, Y. Kafri, and A. P. Solon, Bodies in an interacting active fluid: far-field influence of a single body and interaction between two bodies, *Journal of Statistical Mechanics: Theory and Experiment* **2020**, 063211 (2020).
 - [23] S. Ro, Y. Kafri, M. Kardar, and J. Tailleur, Disorder-induced long-ranged correlations in scalar active matter, *Physical Review Letters* **126**, 048003 (2021).
 - [24] Y. B. Dor, S. Ro, Y. Kafri, M. Kardar, and J. Tailleur, The far-reaching influence of boundaries on shaping bulk behavior of active matter, *arXiv preprint arXiv:2108.13409* (2021).
 - [25] C. M. Rohwer, M. Kardar, and M. Krüger, Activated diffusiophoresis, *The Journal of Chemical Physics* **152**, 084109 (2020).

- [26] P. Galajda, J. Keymer, P. Chaikin, and R. Austin, A wall of funnels concentrates swimming bacteria, *Journal of bacteriology* **189**, 8704 (2007).
- [27] N. Nikola, A. P. Solon, Y. Kafri, M. Kardar, J. Tailleur, and V. R., Active Particles with Soft and Curved Walls: Equation of State, Ratchets, and Instabilities., *Physical Review Letters* **117**, 098001 (2016).
- [28] S. Takatori, W. Yan, and J. Brady, Swim Pressure: Stress Generation in Active Matter, *Physical Review Letters* **113**, 028103 (2014).
- [29] X. Yang, M. Manning, and M. Marchetti, Aggregation and segregation of confined active particles, *Soft Matter* **10**, 6477 (2014).
- [30] A. P. Solon, J. Stenhammar, R. Wittkowski, M. Kardar, Y. Kafri, M. E. Cates, and J. Tailleur, Pressure and Phase Equilibria in Interacting Active Brownian Spheres, *Physical Review Letters* **114**, 198301 (2015).
- [31] Y. Fily, Y. Kafri, A. P. Solon, J. Tailleur, and A. Turner, Mechanical pressure and momentum conservation in dry active matter, *Journal of Physics A: Mathematical and Theoretical* **51**, 044003 (2017).
- [32] J. Elgeti and G. Gompper, Self-propelled rods near surfaces, *EPL (Europhysics Letters)* **85**, 38002 (2009).
- [33] J. Elgeti and G. Gompper, Wall accumulation of self-propelled spheres, *EPL (Europhysics Letters)* **101**, 48003 (2013).
- [34] C. F. Lee, Active particles under confinement: aggregation at the wall and gradient formation inside a channel, *New Journal of Physics* **15**, 055007 (2013).
- [35] Y. Fily, A. Baskaran, and M. Hagan, Dynamics and density distribution of strongly confined noninteracting non-aligning self-propelled particles in a nonconvex boundary, *Physical Review E* **91**, 012125 (2015).
- [36] B. Ezhilan, R. Alonso-Matilla, and D. Saintillan, On the distribution and swim pressure of run-and-tumble particles in confinement, *Journal of Fluid Mechanics* **781** (2015).
- [37] C. G. Wagner, M. F. Hagan, and A. Baskaran, Steady-state distributions of ideal active Brownian particles under confinement and forcing, *Journal of Statistical Mechanics: Theory and Experiment* **2017**, 043203 (2017).
- [38] C. G. Wagner, M. F. Hagan, and A. Baskaran, Steady states of active brownian particles interacting with boundaries, *Journal of Statistical Mechanics: Theory and Experiment* **2022**, 013208 (2022).
- [39] In the semi-infinite system we consider here, $\delta\rho(\mathbf{r})$ vanishes at infinity. In a finite system, one would need to consider $\rho = z\rho_{FW} + \delta\rho$ to ensure the proper normalization of the density field.
- [40] J. Kevorkian, *Partial Differential Equations: Analytical Solution Techniques*, 2nd ed., Texts in Applied Mathematics No. 35 (Springer, 2000).
- [41] J. D. Jackson, *Classical electrodynamics*, 3rd ed. (Wiley, New York, NY, 1999).
- [42] The divergence of the force is negative throughout the domain, $\nabla \cdot \mathbf{F} < 0$, in principle allowing for possible stable fixed points if $\mathbf{F} = 0$.
- [43] A. P. Solon, M. E. Cates, and J. Tailleur, Active brownian particles and run-and-tumble particles: A comparative study, *The European Physical Journal Special Topics* **224**, 1231 (2015).
- [44] J. Tailleur and M. Cates, Statistical mechanics of interacting run-and-tumble bacteria, *Physical Review Letters* **100**, 218103 (2008).
- [45] A. Dhar, A. Kundu, S. N. Majumdar, S. Sabhapandit, and G. Schehr, Run-and-tumble particle in one-dimensional confining potentials: steady-state, relaxation, and first-passage properties, *Physical Review E* **99**, 032132 (2019).
- [46] N. Ierushalmi, M. Malik-Garbi, A. Manhart, E. A. Shah, B. L. Goode, A. Mogilner, and K. Keren, Centering and symmetry breaking in confined contracting actomyosin networks, *Elife* **9**, e55368 (2020).
- [47] M. Wühr, S. Dumont, A. C. Groen, D. J. Needleman, and T. J. Mitchison, How does a millimeter-sized cell find its center?, *Cell cycle* **8**, 1115 (2009).
- [48] T. Mitchison, M. Wühr, P. Nguyen, K. Ishihara, A. Groen, and C. M. Field, Growth, interaction, and positioning of microtubule asters in extremely large vertebrate embryo cells, *Cytoskeleton* **69**, 738 (2012).
- [49] J. Xie and N. Minc, Cytoskeleton force exertion in bulk cytoplasm, *Frontiers in cell and developmental biology*, 69 (2020).
- [50] S. W. Grill and A. A. Hyman, Spindle positioning by cortical pulling forces, *Developmental cell* **8**, 461 (2005).
- [51] G. G. Gundersen and H. J. Worman, Nuclear positioning, *Cell* **152**, 1376 (2013).
- [52] F. Farrell, M. Marchetti, D. Marenduzzo, and J. Tailleur, Pattern formation in self-propelled particles with density-dependent motility, *Physical review letters* **108**, 248101 (2012).
- [53] A. P. Solon, J. Stenhammar, M. E. Cates, Y. Kafri, and J. Tailleur, Generalized thermodynamics of phase equilibria in scalar active matter, *Physical Review E* **97**, 020602 (2018).
- [54] J. Irving and J. G. Kirkwood, The statistical mechanical theory of transport processes. iv. the equations of hydrodynamics, *The Journal of chemical physics* **18**, 817 (1950).
- [55] M. Krüger, A. Solon, V. Démery, C. M. Rohwer, and D. S. Dean, Stresses in non-equilibrium fluids: Exact formulation and coarse-grained theory, *The Journal of chemical physics* **148**, 084503 (2018).